
MATHEMATICAL
PHYSICS

Numerical Simulation of Gas Mixtures Based on the Quasi-Gasdynamics Approach as Applied to the Interaction of a Shock Wave with a Gas Bubble

T. G. Elizarova^{a,*} and E. V. Shil'nikov^{a,**}

^a Federal Research Center Keldysh Institute of Applied Mathematics, Russian Academy of Sciences,
Moscow, 125047 Russia

*e-mail: telizar@mail.ru

**e-mail: shilnikov@imamod.ru

Received April 21, 2020; revised July 2, 2020; accepted September 18, 2020

Abstract—A new numerical algorithm for simulating transonic flows of nonreacting gas mixtures is proposed. The algorithm is based on the finite volume method as applied to regularized, or quasi-gasdynamics, equations. The equations describing multicomponent gas flows are derived phenomenologically using an existing regularized system for one-component gas and classical equations for gas mixtures. The numerical examples include the computation of the nonstationary interaction of gas flow with heavy and light gas bubbles.

Keywords: gas mixture, quasi-gasdynamics equations, finite volume method, transonic flows, gas bubbles

DOI: 10.1134/S0965542521010048

INTRODUCTION

The quasi-gasdynamics (QGD), or regularized, equations for describing gas flows of various natures were derived more than thirty years ago and were successfully used to construct numerical algorithms for both traditional computer systems and massively parallel ones (see [1–3]). Estimates show that the QGD approach is especially efficient for the simulation of unsteady or transient gas flows. At present, the use of this approach has been additionally supported by the fact that QGD algorithms are included in the free open-source OpenFOAM toolbox and is available to the user community in Russia and abroad (see [4–6]).

It seems natural to extend the family of QGD algorithms to unsteady multicomponent gas flows. In this work, for the simulation of gas mixture flows, we construct and test a QGD algorithm whose structure is similar that of QGD-based modules available in OpenFOAM. Due to this fact, the new module for multicomponent flow computations will be easy to incorporate into OpenFOAM and to combine it with numerous extensions of gasdynamic techniques available in the toolbox. Specifically, these are modules for turbulent flow computation, simulation of chemical reactions between components, and constantly improved methods for parallelization of the entire technique on modern computer systems.

There are countless engineering problems including simulation of fluid flows of various compositions and natures. Examples are the mixing gas flows in reactors, gas outflow in pipeline accidents, the mixing of gases for their effective combustion, and numerous others. Accordingly, the simulation of multicomponent gas flows is undoubtedly of practical importance, and so are the results described below.

This paper is organized as follows. A mathematical model describing a gas mixture without chemical reactions is presented in Section 1. The model is based on a well-known one-liquid model describing a gas mixture by a system of equations for the densities of individual components, together with momentum and total energy equations common for both components, without explicit description of phase boundaries. To simplify the presentation, we assume that the mixture consists of two ideal gases. In Section 2, a regularized analogue of this system of equations is derived relying on phenomenological considerations. The problem of a shock wave interacting with a gas bubble is formulated in Section 3. Additionally, the principles underlying the numerical implementation of the algorithm are briefly described in this section. Numerical results are described in detail in Section 4. We consider light and heavy gas bubbles placed in

air flow with a shock wave propagating in it. Concluding remarks concerning the presented results are given at the end of this paper.

1. SYSTEM OF EQUATIONS DESCRIBING MULTICOMPONENT GAS FLOW

A gas mixture without chemical reactions is considered within the framework of a well-known model. In this model, the density of each species of the mixture satisfies its own continuity equation. It is assumed that molecules of different species interact quickly comparing to hydrodynamic times, so the velocity and temperature in the flow are identical for the species of the mixture. Accordingly, the momentum and total energy equations are written for the mixture as a whole without considering equations for each species separately. Viscosity and heat conduction are treated for the mixture as a whole and are determined by the viscosity coefficient and thermal conductivity for the mixture.

The equation for the density of the mixture is split into equations for the densities of individual components without explicit description of phase boundaries. Accordingly, the model does not involve a separate equation for determining phase boundaries between the species and they are formed automatically in domains with high gradients of species concentrations. The mutual diffusion between the species of the mixture is not taken into account.

This model is rather often used to describe multicomponent gas flows. Specifically, it was applied by Abgrall and Karni, for example, in [7–10]. For models of this type, much effort was focused on the suppression of spurious oscillations arising at the interface of fluids in the case of using higher order accurate schemes. Double flux modifications of widespread numerical methods, such as TVD-MUSCL [9], discontinuous Galerkin methods [11], and Godunov schemes [12, 13], were applied for this purpose. In contrast to the above-described model, in the multifluid model considered in [12], each fluid has not only its own density, but also its own velocity and pressure. As a result, exchange terms appear on the right-hand sides of the equations. This model is well suited for flow simulation of a mixture of fluids and gases. However, the exchange terms lead to the necessity of integrating a generally stiff ODE system at every step, which significantly complicates the algorithm. In the case of reacting gases, a stiff ODE system has to be solved because of the widely different rates of chemical reactions (see [13, 14]), but, in the absence of chemical reactions, it is desirable to avoid this complication.

For brevity, we consider a mixture of two gases, a and b . In this case, the model described above is represented in the form of the following system of equations:

$$\frac{\partial \rho_a}{\partial t} + \operatorname{div}(\rho_a \mathbf{u}) = 0, \tag{1}$$

$$\frac{\partial \rho_b}{\partial t} + \operatorname{div}(\rho_b \mathbf{u}) = 0, \tag{2}$$

$$\frac{\partial \rho \mathbf{u}}{\partial t} + \operatorname{div}(\rho(\mathbf{u} \otimes \mathbf{u})) + \nabla p = \operatorname{div} \Pi_{\text{NS}} + \rho \mathbf{F}, \tag{3}$$

$$\frac{\partial E}{\partial t} + \operatorname{div}((E + p)\mathbf{u}) = -\operatorname{div} \mathbf{q}_{\text{NS}} + \operatorname{div}(\Pi_{\text{NS}} \cdot \mathbf{u}) + \rho(\mathbf{u} \cdot \mathbf{F}) + Q. \tag{4}$$

This system makes use of the standard notation for gasdynamic quantities. Additionally, the vector \mathbf{F} and the scalar Q are used to denote a specific external force and an external source or sink of energy, respectively. The last is important in the case of reacting gases, which is not included in this consideration. The Navier–Stokes viscous stress tensor Π_{NS} and the heat flux \mathbf{q}_{NS} in the form of Fourier’s law have the traditional form:

$$\Pi_{\text{NS}} = \mu \left((\nabla \otimes \mathbf{u}) + (\nabla \otimes \mathbf{u})^T - \frac{2}{3} \mathbf{I} \operatorname{div} \mathbf{u} \right), \quad \mathbf{q}_{\text{NS}} = -\kappa \nabla T,$$

where \mathbf{I} is the identity matrix. In the presented model, it is assumed that the gas mixture has a unified velocity \mathbf{u} and temperature T , while the density, pressure, and specific total energy of the mixture are determined by the parameters of its components as

$$\rho = \rho_a + \rho_b, \quad p = p_a + p_b, \quad E = \rho \varepsilon + \rho \mathbf{u}^2 / 2.$$

Additionally, the gasdynamic mixture satisfies usual relations for a polytropic ideal gas:

$$p = \rho RT = \rho \varepsilon (\gamma - 1),$$

where γ is the ratio of specific heats of the mixture, R is the gas constant, and ε is the specific internal energy of the mixture:

$$R = \frac{R_a \rho_a + R_b \rho_b}{\rho} = c_p - c_v, \quad \gamma = \frac{c_p}{c_v}, \quad \gamma - 1 = \frac{R}{c_v},$$

$$\varepsilon = \frac{\varepsilon_a \rho_a + \varepsilon_b \rho_b}{\rho} = c_v T, \quad c_v = \frac{c_{va} \rho_a + c_{vb} \rho_b}{\rho}.$$

It should be emphasized that the thermodynamic mixture parameters c_p and c_v and, hence, R and γ are not constants, in contrast to their counterparts for an ideal polytropic gas, but are determined in terms of weighted parameter values of the mixture. They depend on the density of each gas species at each spatio-temporal point (\mathbf{x}, t) .

The speed of sound for the mixture can be computed using the relation

$$\rho c_s^2 = \gamma_a p_a + \gamma_b p_b.$$

Obviously, the model described is easy to generalize to mixtures with a larger number of gas components.

2. REGULARIZED SYSTEM OF EQUATIONS FOR DESCRIBING MULTICOMPONENT GAS FLOW

The regularized (or QGD) equations for describing the flow of a viscous polytropic ideal gas have the form (see, e.g., [2, 3])

$$\frac{\partial \rho}{\partial t} + \operatorname{div}(\rho(\mathbf{u} - \mathbf{w})) = 0, \quad (5)$$

$$\frac{\partial \rho \mathbf{u}}{\partial t} + \operatorname{div}(\rho(\mathbf{u} - \mathbf{w}) \otimes \mathbf{u}) + \nabla p = \operatorname{div} \Pi + (\rho - \tau \operatorname{div}(\rho \mathbf{u})) \mathbf{F}, \quad (6)$$

$$\frac{\partial E}{\partial t} + \operatorname{div}((E + p)(\mathbf{u} - \mathbf{w})) = -\operatorname{div} \mathbf{q} + \operatorname{div}(\Pi \cdot \mathbf{u}) + \rho(\mathbf{u} - \mathbf{w}) \cdot \mathbf{F} + Q. \quad (7)$$

This system of equations includes regularizing additions of the form

$$\mathbf{w} = \frac{\tau}{\rho} (\operatorname{div}(\rho \mathbf{u} \otimes \mathbf{u}) + \nabla p - \rho \mathbf{F}), \quad (8)$$

$$\hat{\mathbf{w}} = \frac{\tau}{\rho} (\rho(\mathbf{u} \nabla) \mathbf{u} + \nabla p - \rho \mathbf{F}), \quad (9)$$

$$\mathbf{q} = \mathbf{q}_{\text{NS}} + \mathbf{q}^\tau, \quad (10)$$

$$\Pi = \Pi_{\text{NS}} + \rho \mathbf{u} \otimes \hat{\mathbf{w}} + \tau(\mathbf{u} \nabla p + \gamma p \operatorname{div} \mathbf{u} - (\gamma - 1)Q), \quad (11)$$

$$-\mathbf{q}^\tau = \tau \rho \mathbf{u} \left(\mathbf{u} \nabla \varepsilon + p(\mathbf{u} \nabla) \left(\frac{1}{\rho} \right) - \frac{Q}{\rho} \right). \quad (12)$$

All these additions are proportional to the small coefficient τ , which has the dimension of time and, for gas flows, can be represented in the form

$$\tau = l/c_s, \quad (13)$$

where c_s is the speed of sound and l is a characteristic length determined by the problem under consideration. In most computational problems, it is convenient to define the characteristic length as the spatial mesh size h :

$$\tau = \alpha h/c_s, \quad (14)$$

where $\alpha \leq 1$ is a numerical coefficient, which is specified in the course of problem solving depending on the accuracy and stability of the numerical algorithm. The coefficient τ determines the subgrid-scale dissipation of the algorithm and is closely related to the stability condition for the algorithm.

It should be emphasized that the additional terms are additions to the velocity \mathbf{u} , the viscous stress tensor Π_{NS} , and the heat flux \mathbf{q}_{NS} . The introduction of the regularizing additions into system (5)–(7) ensures

that the mass, momentum, energy, and angular momentum conservation laws are satisfied and the dissipative function is nonnegative.

Regularized equations for a mixture can be written by analogy with the QGD equations (5)–(7) for a single-component gas. As in system (1)–(4), we set $\rho = \rho_a + \rho_b$ and split the continuity equation (5) into ones for each of the species ρ_a and ρ_b . Accordingly, the regularizer involved in the original equation for the total density of the mixture is split as well. Since the species of the mixture have identical velocities, we assume that the regularizing additions to the species velocities are also identical: $\mathbf{w}_a = \mathbf{w}_b = \mathbf{w}$. Then the regularized (or QGD) system of equations for the gas mixture has the form

$$\frac{\partial \rho_a}{\partial t} + \operatorname{div}(\rho_a(\mathbf{u} - \mathbf{w})) = 0, \quad (15)$$

$$\frac{\partial \rho_b}{\partial t} + \operatorname{div}(\rho_b(\mathbf{u} - \mathbf{w})) = 0, \quad (16)$$

$$\frac{\partial \rho \mathbf{u}}{\partial t} + \operatorname{div}(\rho(\mathbf{u} - \mathbf{w}) \otimes \mathbf{u}) + \nabla p = \operatorname{div} \Pi + (\rho - \tau \operatorname{div}(\rho \mathbf{u}))\mathbf{F}, \quad (17)$$

$$\frac{\partial E}{\partial t} + \operatorname{div}((E + p)(\mathbf{u} - \mathbf{w})) = -\operatorname{div} \mathbf{q} + \operatorname{div}(\Pi \cdot \mathbf{u}) + \rho(\mathbf{u} - \mathbf{w}) \cdot \mathbf{F} + Q. \quad (18)$$

This system is supplemented with regularizing additions of form (8)–(12). The coefficient τ is calculated in terms of the mixture speed of sound c_s using relation (13) or (14).

The regularized equations given above are derived phenomenologically, and their mathematical properties are not examined in detail. However, the first computations based on these equations performed for the problem of Rayleigh–Taylor instability (see [15]) demonstrated the high performance and stability of the numerical algorithm used. The computational capabilities of this model for transonic flows are shown in Section 4.

To conclude this section, we note that other QGD-based regularized systems of equations for describing mixtures of nonreacting gases have been constructed and tested in numerical experiments.

The first system of equations of this class (see, e.g., [2, 16]) was intended for rarefied gas flows. This system represented a two-fluid model with its own continuity, momentum, and total energy equations written for each species of the mixture. The equations were related via exchange terms that appeared on the right-hand sides of the momentum and energy equations and ensured momentum and energy exchange between the species of the mixture. Significant improvements to this system of equations were made in [17]. Specifically, the system was written in the form of conservation laws, an entropy transport equation with a nonnegative dissipative function was derived for it, and the exchange terms were generalized to polyatomic gases. The physical interpretation of the exchange terms in the case of polyatomic gases was given in [18].

However, an analysis and experience of numerical simulation showed that the two-fluid system with exchange terms is ineffective as applied to rather dense gases. In the case of dense gases, the regularizing additions were significantly modified and two new systems of equations for gas mixtures were obtained (see [19]). For them, mass, kinetic and internal energy balance equations, and new total entropy balance equations were derived, and the nonnegativity of entropy production was proved. However, the resulting equations contain additional nonconservative terms in the total energy equation, which leads to difficulties in their numerical implementation.

A similar (in structure) simpler quasi-hydrodynamic mixture model was constructed in [20] for the simulation of slow two-phase flows in porous media with allowance for interphase interactions. The form of this system of equations is given in [19].

3. FORMULATION OF THE PROBLEM OF A GAS BUBBLE INTERACTING WITH A SHOCK WAVE

The test problem is to simulate the interaction of a plane shock wave moving in air with a cylindrical bubble of another gas. Such an experiment was described in [21] and was numerically studied in [7, 8, 22, 23]. Consider a two-dimensional rectangular domain filled with air (Fig. 1). A plane shock wave propagates through the air and impinges on a cylindrical bubble of helium or R22 coolant (CHClF_2). The bubble is of radius $R = 0.025$ and is centered at the point $(x_c, y_c) = (0.32, 0)$. Neglecting the boundary effects, i.e., assuming that the cylinder is infinitely long, we can simulate this flow in two dimensions. In the cen-

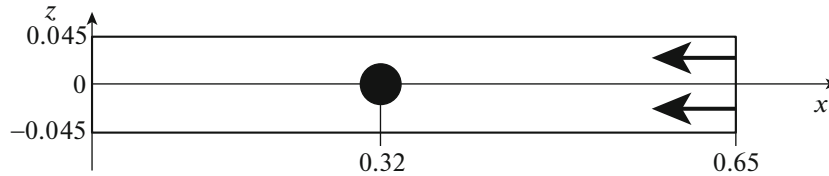


Fig. 1. Schematic view of the computational domain.

tral cross section, the flow is nearly two-dimensional and the boundary effects can be neglected if the length of the cylinder is large as compared with the setup height.

All gas species are assumed to be ideal gases. The gas constant is $R = R_{\text{univ}}/m$, where R_{univ} is the universal gas constant and m is the molecular mass of the gas. We neglect the physical viscosity μ and the thermal conductivity κ of the gases and use the equations of the mixture in the Euler formulation. The external force \mathbf{F} and the heat source Q are assumed to be zero. The initial dynamically equilibrium parameters of the gases in the computational domain are given in Table 1.

At the right boundary, we specify air inflow with parameters behind the shock wave moving from right to left through the air with the velocity corresponding to the Mach number $M_s = 1.22$:

$$(\rho, u, v, p, \gamma)|_{\text{right}} = (1.3764, -124.82414, 0.0, 156983.9256, 1.4).$$

The other boundaries of the domain are assumed to be impermeable solid walls with slip boundary conditions. The computations are performed on rectangular grids, namely, on a coarse grid consisting of 1300×178 cells with spatial step size $h = 5 \times 10^{-4}$ in both directions and on a twice finer grid consisting of 2600×356 cells.

The QGD system (15)–(18) is numerically implemented using an explicit finite-volume scheme with all spatial derivatives approximated by second-order central differences. All gasdynamic variables are placed at cell centers. Their values in the centers of cell faces are calculated using linear interpolation. The stability condition for this scheme has the form of the Courant condition, and the time step is determined using the formula

$$\Delta t = \beta \min_i \frac{h_i}{c_{s_i} + |\mathbf{u}_i|}, \quad (19)$$

where the minimum is taken over all grid cells, i is the cell index, and β is a numerical coefficient (Courant number) independent of the spatial mesh size. The final computation time is specified as $t_{\text{fin}} = 1.4 \times 10^{-3}$ for the helium bubble and $t_{\text{fin}} = 1.1 \times 10^{-3}$ for the R22 bubble. Time is measured in seconds from the moment when the shock wave started its motion from the right boundary of the computational domain.

4. ANALYSIS OF NUMERICAL RESULTS

The computations for the R22 bubble are performed using the scheme parameter $\alpha = 0.4$ and the Courant number $\beta = 0.5$. Figure 2 shows the numerical schlieren images obtained at the sequential times $t = 7.61 \times 10^{-4}$, $t = 8.47 \times 10^{-4}$, $t = 1.01 \times 10^{-3}$, and $t = 1.1 \times 10^{-3}$ (from top to bottom).

The schlieren method is widely used in experiments for visualization of various processes in gas media: in wind tunnels, fluid mechanics, ballistics, the study of gas and solution propagation and mixing, etc. In this context, comparisons with experiment require a numerical analogue of schlieren images. In numerical experiments, this is achieved by depicting a somehow scaled logarithm of the absolute value of the density

Table 1. Initial parameters of the gases. All quantities are given in SI units

| Gas | ρ | u | v | p | γ | m | R | c_s |
|--------|--------|-----|-----|--------|----------|-------|-------|--------|
| Air | 1.0 | 0.0 | 0.0 | 10^5 | 1.4 | 28.96 | 287.1 | 374.16 |
| Helium | 0.182 | 0.0 | 0.0 | 10^5 | 5/3 | 4.003 | 2077 | 915.75 |
| R22 | 3.1538 | 0.0 | 0.0 | 10^5 | 1.249 | 86.47 | 96.15 | 199.0 |

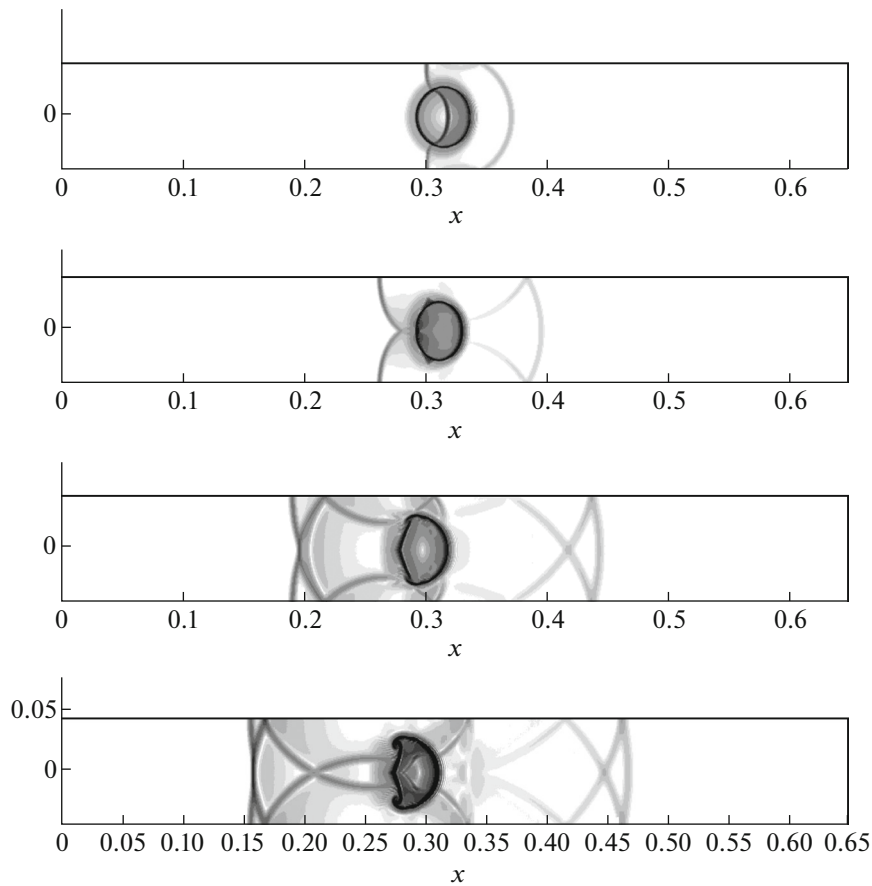


Fig. 2. R22 bubble: numerical schlieren images obtained at the sequential times $t = 7.61 \times 10^{-4}$, $t = 8.47 \times 10^{-4}$, $t = 1.01 \times 10^{-3}$, and $t = 1.1 \times 10^{-3}$ (from top to bottom).

gradient. In this work, we use the capabilities of the Tecplot 360 graphics software package. Scaling is achieved by choosing the ranges of the depicted quantity so that its characteristic features are seen in the best way in the resulting flow pattern.

After the shock wave impinges on the bubble, the latter begins to move to the left and deforms (Fig. 2). In the upper panel corresponding to the time $t = 7.61 \times 10^{-4}$, the incident shock wave consists of two vertical fragments located above and below the bubble. Inside the bubble, we can see a refracted shock wave, which becomes curved due to its lower propagation velocity. This is explained by the fact that the speed of sound in R22 is nearly half as high as in the air (Table 1). Moreover, the external ends of the refracted wave move together with the internal ends of the incident wave fragments. The curved reflected wave is weaker than the incident and refracted ones and propagates to the right of the bubble toward the right boundary of the domain. The wave reflected from the bubble is connected to the incident wave fragments by two weak waves reflected from the horizontal walls. Wave diffraction around the bubble leads to its deformation. The next panels in Fig. 2 show the formation and evolution of two vortices in the upper and lower parts of the bubble, where vorticity appears. Later, after passing the bubble, the fragments of the incident shock wave merge and move as a whole to the left. First lagging behind, the point where the incident wave fragments merge gradually overtakes their external ends and the wavefront becomes straightened (the lower panel in Fig. 2). All these effects agree well with experimental and numerical results of other authors.

The propagation of the refracted wave through the bubble and the corresponding variations in the wave shape can be seen in Fig. 3.

As is noted above, the speed of sound in the R22 gas is much lower than in the air, so the speed of the refracted wave moving in the bubble is less than that of the incident wave moving between the bubble and the walls. Moreover, the outer edges of the refracted wave move over the bubble surface together with the inner edges of the incident wave. As a result, the refracted wave becomes curved and its curvature increases

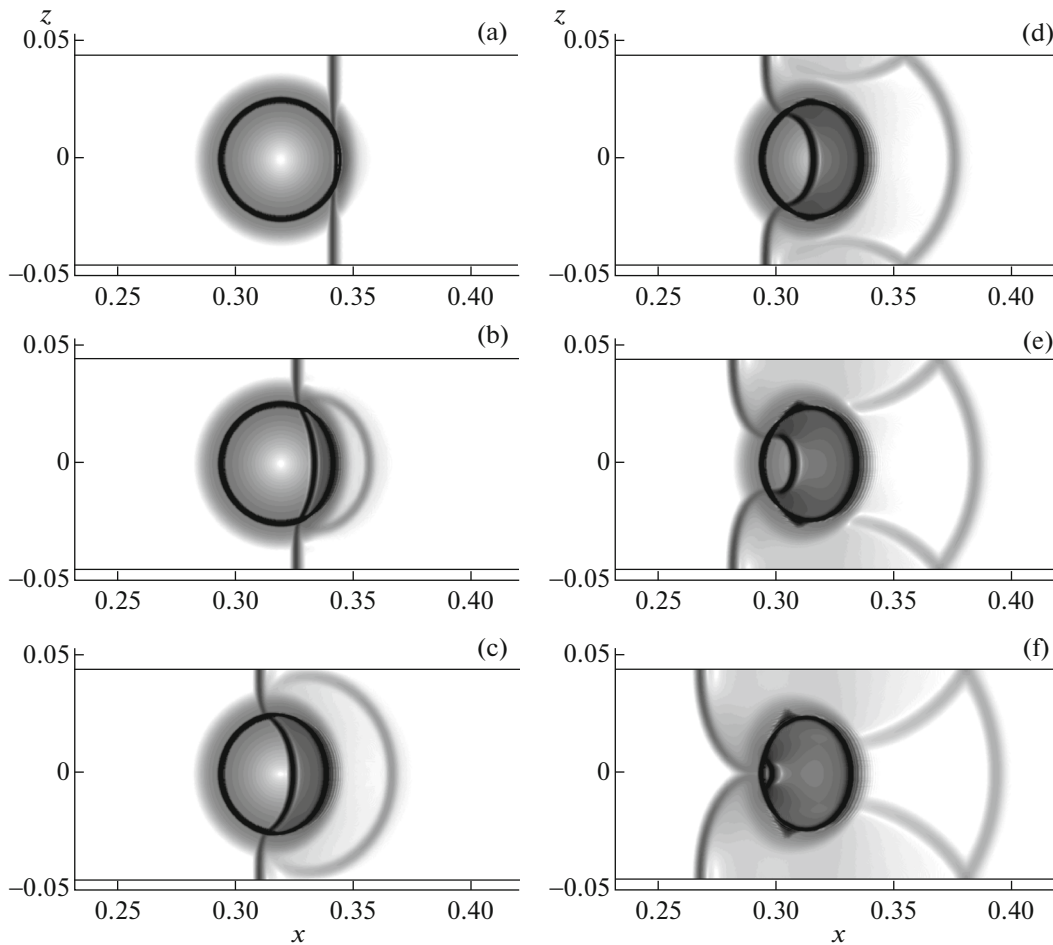


Fig. 3. Shock wave propagating through the R22 bubble.

in the course of motion. For example, the refracted wave in Fig. 3e has the shape of a semicircle, while, in Fig. 3f, it becomes nearly circular. Thus, the bubble of the heavy R22 gas acts on the incident wave as a converging lens.

In Fig. 4, the shape of the bubble obtained at the end of the computations in our study is compared with the numerical results of [7] and the experimental data from [21]. Specifically, the figure shows the shape of the R22 bubble at the final computation time $t = 1.1 \times 10^{-3}$: (a) our results, (b) the results of [7], and (c) the experimental data from [21]. It should be noted that both the evolution of the bubble shape and the general structure of the complicated flow with a large number of waves of different types coincide with the results obtained by these and other authors.

The computations for the helium bubble are performed with the parameter $\alpha = 0.4$ and the Courant number $\beta = 0.2$. The results are shown in Fig. 5, which presents the schlieren images at the sequential times $t = 7.04 \times 10^{-4}$, $t = 7.52 \times 10^{-4}$, $t = 9.13 \times 10^{-4}$, and $t = 1.342 \times 10^{-3}$ (from top to bottom).

In contrast to the preceding case, the helium bubble interacting with the incident shock wave is lighter than the surrounding air, so the bubble acts as a diverging acoustic lens. As a result, the wave structure and the overall flow field differ widely from those observed in the case of the heavy bubble.

By analogy with the previous case, after the incident shock wave collides with the bubble, a curved refracted wave is formed in the latter. However, this wave moves faster than the incident one, since the speed of sound in helium is 2.5 times higher than in the air (Table 1), so its convexity is leftward. Subsequently, the helium bubble is deformed to a much higher degree than the R22 bubble. It can be seen that the upstream side of the bubble is much more flattened even in the upper panel in Fig. 5 and becomes nearly flat in the second panel. Subsequently, it progressively curves leftward and nearly reaches the

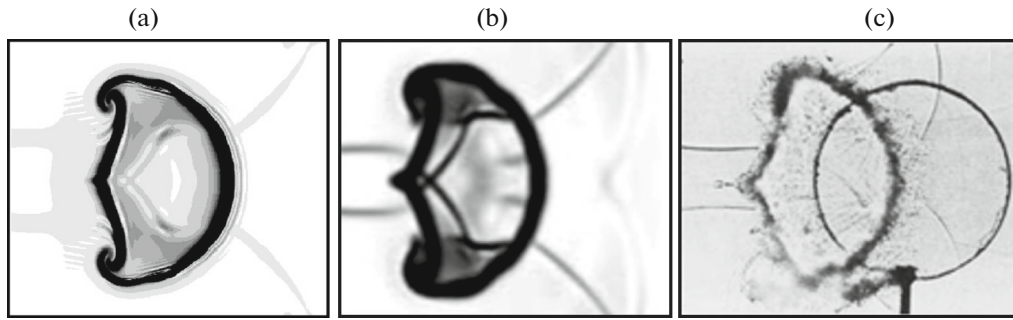


Fig. 4. Shape of the R22 bubble at the final time $t = 1.1 \times 10^{-3}$: (a) our results, (b) the results of [7], and (c) the experimental data from [21].

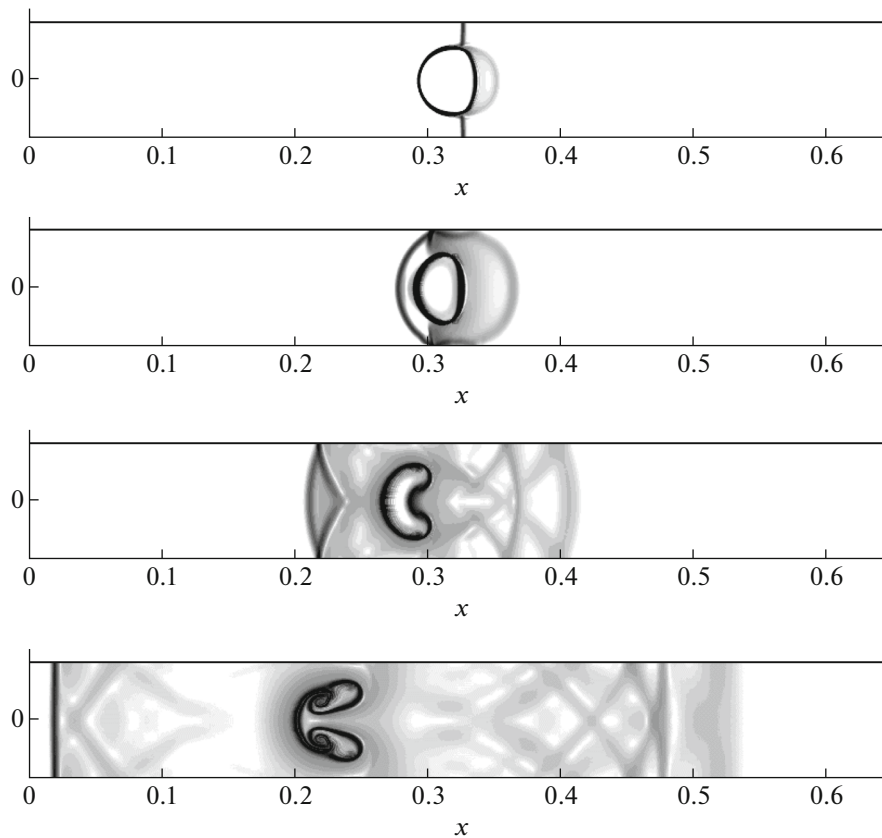


Fig. 5. Helium bubble: numerical schlieren images obtained at the sequential times $t = 7.04 \times 10^{-4}$, $t = 7.52 \times 10^{-4}$, $t = 9.13 \times 10^{-4}$, and $t = 1.342 \times 10^{-3}$ (from top to bottom).

downstream side. As a result, the bubble is, in fact, separated into two parts connected by a thin bridge (the lower panel in Fig. 5). As in the preceding case, in the upper and lower parts of the bubble, there appear vortices with nonzero vorticity. However, in this case, the vortices are located inside the bubble, rather than outside of it. Note also the natural fact that, influenced by the incident wave, the light helium bubble moves to the left faster than the heavy R22 bubble.

The velocity of the refracted wave is so high that we cannot even see in Fig. 5 how it passes through the bubble. Even in the upper panel in Fig. 5, this wave reaches the left boundary of the bubble. To observe how the refracted wave moves inside the bubble, Fig. 6 presents flow field fragments at earlier close times,

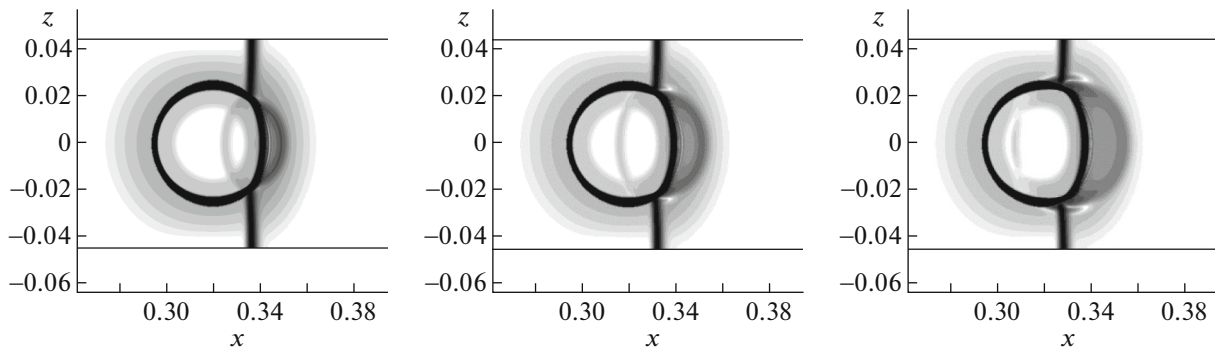


Fig. 6. Refracted wave propagating through the helium bubble at the times $t = 6.86 \times 10^{-4}$, $t = 6.95 \times 10^{-4}$, and $t = 7.03 \times 10^{-4}$ (from left to right).

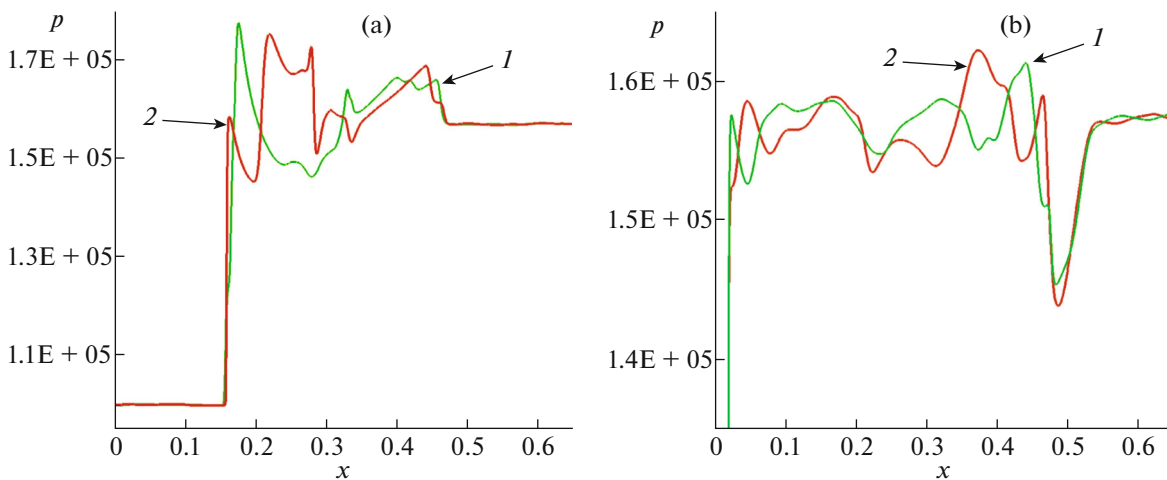


Fig. 7. Pressure profiles along the line (1) $z = 0$ and (2) $z = 0.4$ for the (a) R22 and (b) helium bubble.

namely, at $t = 6.86 \times 10^{-4}$, $t = 6.95 \times 10^{-4}$, and $t = 7.03 \times 10^{-4}$ (from left to right). It can be seen that the incident wave hardly moves over the time required for the refracted wave to propagate through the entire bubble.

Another difference from the preceding case is that the reflected wave is a rarefaction one, rather than a shock. This is well seen in Fig. 7, which depicts the pressure profiles at the final computation time along the central line $z = 0$ (curves 1) and the line $z = 0.4$ (curves 2), which passes between the wall and the bubble for both variants of computations.

In the case of R22 (Fig. 7a), the pressure in the wave propagating upstream is higher than the background value (the horizontal segment near the right boundary of the domain is preceded by an increase in pressure), while, in the case of helium (see Fig. 7b), the pressure is lower than its background value, namely, a decrease in pressure is observed to the left of the horizontal pressure segment. This difference in the pressure behavior is explained by the fact that, at the moment when the shock wave impinges on the bubble, the heavy R22 bubble acts as a nearly solid wall, while the light helium bubble plays the role of an almost vacuum.

In Fig. 8, the shape of the helium bubble obtained at the final computation time in our study is compared with its counterparts as in the R22 case. More specifically, the bubble shape is shown at the time $t = 1.342 \times 10^{-3}$: (a) our results, (b) the results of [7], and (c) the experimental data from [21].

Our numerical results show that the numerical approach used is highly efficient and accurate. The overall flow pattern and the basic characteristic features of the complicated flows agree well with both

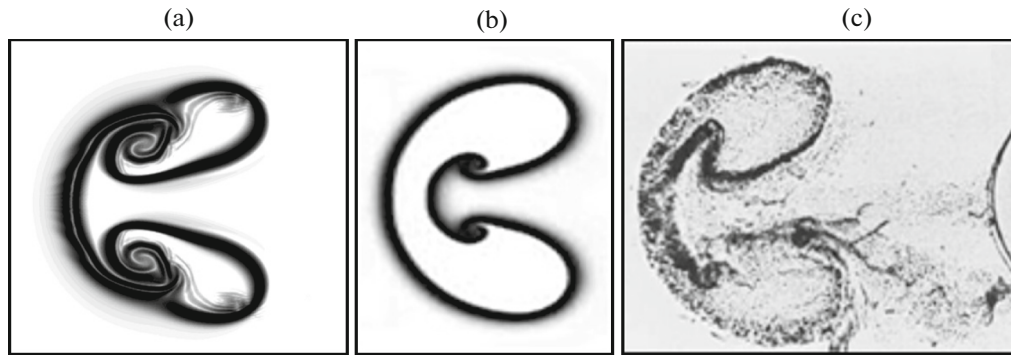


Fig. 8. Shape of the helium bubble at the time $t = 1.342 \times 10^{-3}$: (a) our results, (b) the results of [7], and (c) the experimental data from [21].

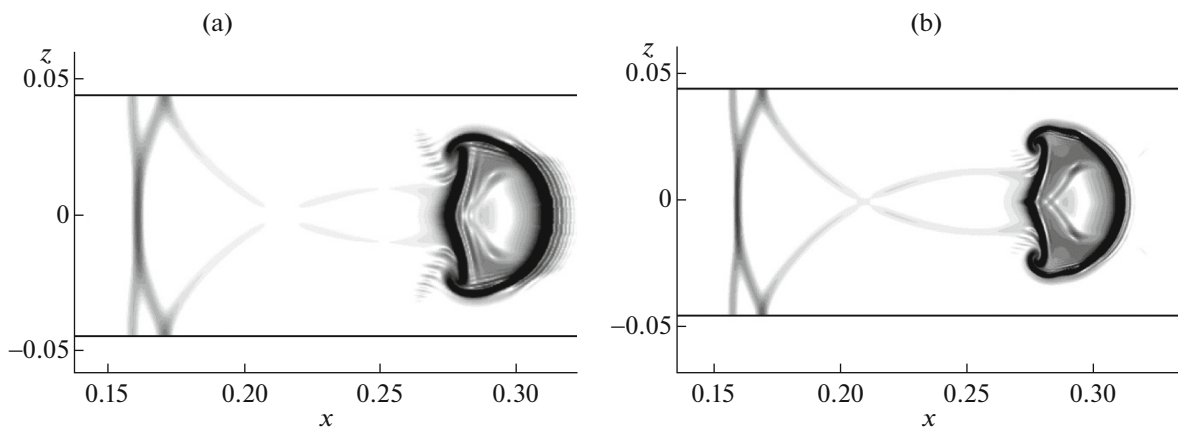


Fig. 9. Numerical schlieren images at the time $t = 1.1 \times 10^{-3}$ obtained on (a) 1300×178 and (b) 2600×356 grids.

experimental and numerical results of other authors. Note also that the numerical solution has the correct symmetry.

The results obtained on different spatial grids are compared in Fig. 9, which presents the schlieren images for the R22 bubble produced at the final computation time $t = 1.1 \times 10^{-3}$ on grids consisting of (a) 1300×178 and (b) 2600×356 cells. It can be seen that, under mesh refinement, the general flow structure is preserved and its quality improves. The waves become thinner and more pronounced, and subtler flow features are manifested, especially inside the bubble. A decrease in the regularization parameter α has nearly the same effect on the solution as mesh refinement. However, the stability of the scheme degrades and a smaller time step is required. For this reason, the computations are performed at the minimum value of α ensuring stability at a reasonable value of the Courant number β .

Note also that the results of [7] used for comparison with ours were obtained using a much more complicated difference scheme on a dynamically adaptive built-in grid equivalent to a uniform one consisting of 16000×800 cells, which is finer by one order of magnitude than the grid used in our work. To estimate the performance of the algorithm, we note, for example, that the computations on a personal computer on a fine 2600×356 grid (with about a million cell) in the case of the heavy bubble required about 10 h CPU time.

CONCLUDING REMARKS

An efficient algorithm for the numerical simulation of multicomponent gas flows without chemical reactions is presented. Regularized (or QGD) equations underlying the algorithm are derived phenomenologically. They are close in form to the corresponding regularized equations for one-component gases.

The constructed algorithm makes it possible to reproduce subtle effects arising in the nonstationary interaction of a shock wave with light and heavy gas bubbles. The algorithm was also used to model the Rayleigh–Taylor instability in a wide range of Atwood numbers (see [15]). Thus, the numerical results suggest the high performance of the algorithm.

Due to its structure, the algorithm can be naturally generalized to multicomponent mixtures of ideal gases.

Since the given method is closely related to QGD algorithms for computing one-component gas flows, it can be naturally generalized to unstructured meshes and flows with sources and, by analogy with the QGD algorithm, can be incorporated into the open-source OpenFOAM package as a new original computational core.

REFERENCES

1. B. N. Chetverushkin, *Kinetic Schemes and Quasi-Gasdynamic System of Equations* (MAKS, Moscow, 2004; CIMNE, Barcelona, 2008).
2. T. G. Elizarova, *Quasi-Gas Dynamic Equations* (Nauchnyi Mir, Moscow, 2007; Springer, Berlin, 2009).
3. Yu. Sheretov, *Continuum Dynamics under Spatiotemporal Averaging* (Regulyarnaya i Khaoticheskaya Dinamika, Moscow–Izhevsk, 2009) [in Russian].
4. M. V. Kraposhin, D. A. Ryazanov, E. V. Smirnova, T. G. Elizarova, and M. A. Istomina, “Development of OpenFOAM solver for compressible viscous flows simulation using quasi-gas dynamic equations,” *IEEE eXplore* **29** (6), 117–124 (2017).
5. M. V. Kraposhin, E. V. Smirnova, T. G. Elizarova, and M. A. Istomina, “Development of a new OpenFOAM solver using regularized gas dynamic equations,” *Comput. Fluids* **166**, 163–175 (2018).
6. *OpenFOAM User Guide, Version 7*. <https://cfd.direct/openfoam/user-guide/>
7. J. Quirk and S. Karni, “On the dynamics of a shock-bubble interaction,” *J. Fluid Mech.* **318**, 129–163 (1996).
8. R. Abgrall, “How to prevent pressure oscillations in multicomponent flow calculations: A quasi conservative approach,” *J. Comput. Phys.* **125**, 150–160 (1996).
9. R. Abgrall and S. Karni, “Computations of compressible multifluids,” *J. Comput. Phys.* **169**, 594–623 (2001).
10. G. Billet and R. Abgrall, “An adaptive shock-capturing algorithm for solving unsteady reactive flows,” *Comput. Fluids* **32**, 1473–1495 (2003).
11. G. Billet and J. Ryan, “A Runge–Kutta discontinuous Galerkin approach to solve reactive flows: The hyperbolic operator,” *J. Comput. Phys.* **230**, 1064–1083 (2011).
12. R. Saurel and R. Abgrall, “A multiphase Godunov method for compressible multifluid and multiphase flows,” *J. Comput. Phys.* **150**, 425–467 (1999).
13. V. E. Borisov and Yu. G. Rykov, “Modified Godunov method for multicomponent flow simulation,” *J. Phys.: Conf. Ser.*, No. 1250, 012006 (2019).
14. Y. S. Lian and K. Xu, “A gas-kinetic scheme for multimaterial flows and its application in chemical reactions,” *J. Comput. Phys.* **163**, 349–375 (2000).
15. E. V. Shilnikov and T. G. Elizarova, “Numerical simulation of gravity instabilities in gas flows by use of the quasi gas dynamic equation system,” *IOP Conf. Ser. Mater. Sci. Eng.* **657**, 012035 (2019).
16. T. G. Elizarova, I. A. Graur, and J.-C. Lengrand, “Two-fluid computational model for a binary gas mixture,” *Eur. J. Mech. B* **3**, 351–369 (2001).
17. T. G. Elizarova, A. A. Zlotnik, and B. N. Chetverushkin, “On quasi-gasdynamic and quasi-hydrodynamic equations for binary gas mixtures,” *Dokl. Math.* **90** (3), 719–723 (2014).
18. T. G. Elizarova and J.-C. Lengrand, “Free parameters for the modelization of nonmonatomic binary gas mixtures,” *J. Thermophys. Heat Transfer* **30** (3), 695–697 (2016).
19. T. G. Elizarova, A. A. Zlotnik, and E. V. Shil'nikov, “Regularized equations for numerical simulation of flows of homogeneous binary mixtures of viscous compressible gases,” *Comput. Math. Math. Phys.* **59** (11), 1832–1847 (2019).
20. V. A. Balashov and E. B. Savenkov, “Quasi-hydrodynamic model of multiphase fluid flows taking into account phase interaction,” *J. Appl. Mech. Tech. Phys.* **59** (3), 434–444 (2018).
21. J. F. Haas and B. Sturtevant, “Interaction of weak shock waves with cylindrical and spherical gas inhomogeneities,” *J. Fluid Mech.* **181**, 41–76 (1987).
22. I. E. Ivanov and I. A. Kryukov, “Numerical modeling of multicomponent gas flows with strong discontinuities of medium properties,” *Mat. Model.* **19** (12), 89–100 (2007).
23. V. E. Borisov and Yu. G. Rykov, “Simulation of multicomponent gas flows using the double-flux method,” *Mat. Model.* **32** (10), 3–20 (2020).

Translated by I. Ruzanova